Superconducting gatemon qubit based on a proximitized two-dimensional electron gas

Lucas Casparis[1,8], Malcolm R. Connolly[1,8], Morten Kjaergaard[1,7], Natalie J. Pearson[1,2], Anders Kringhøj[1], Thorvald W. Larsen[1], Ferdinand Kuemmeth[1], Tiantian Wang[3,4], Candice Thomas[3,4], Sergei Gronin[4], Geoffrey C. Gardner[4], Michael J. Manfra[3,4,5,6], Charles M. Marcus[1] and Karl D. Petersson[1*]

The coherent tunnelling of Cooper pairs across Josephson junctions (JJs) generates a nonlinear inductance that is used extensively in quantum information processors based on superconducting circuits, from setting qubit transition frequencies[1] and interqubit coupling strengths[2] to the gain of parametric amplifiers[3] for quantum-limited readout. The inductance is either set by tailoring the metal oxide dimensions of single JJs, or magnetically tuned by parallelizing multiple JJs in superconducting quantum interference devices with local current-biased flux lines. JJs based on superconductor–semiconductor hybrids represent a tantalizing all-electric alternative. The gatemon is a recently developed transmon variant that employs locally gated nanowire superconductor–semiconductor JJs for qubit control[4,5]. Here we go beyond proof-of-concept and demonstrate that semiconducting channels etched from a wafer-scale two-dimensional electron gas (2DEG) are a suitable platform for building a scalable gatemon-based quantum computer. We show that 2DEG gatemons meet the requirements[6] by performing voltage-controlled single qubit rotations and two-qubit swap operations. We measure qubit coherence times up to ~2 μs, limited by dielectric loss in the 2DEG substrate.

Figure 1a shows an optical micrograph of a typical device that hosts six two-dimensional electron gas (2DEG) gatemon qubits. Each gatemon comprises an Al island shunted to the ground plane via a 2DEG Josephson junction (JJ) and capacitively coupled to a serpentine-shaped coplanar waveguide cavity. The self-capacitance C of the island together with the nonlinear inductance of the JJ creates an anharmonic potential for plasmon oscillations across the JJ. The ground $|0\rangle$ and excited $|1\rangle$ states of the qubit correspond to the lowest two harmonic oscillator states, which in the transmon limit ($E_J \gg E_C$) are separated in energy by a transition frequency $f_Q \approx \sqrt{8E_C E_J} / h$, where $E_C = e^2/2C$ is the charging energy and E_J is the Josephson energy[1,7].

Fixed-frequency transmons that employ single metal-oxide JJs benefit from longer coherence times, but at the cost of slow (~150 ns) two-qubit gate operation times[8] and frequency crowding[9]. Frequency-tunable qubits allow faster two-qubit gates, but the susceptibility to flux noise in superconducting quantum interference devices (SQUIDs) results in typical phase coherence times

of $T_2^* \approx 5\,\mu s$ (refs [9,10]). Moreover, the milliampere currents used to control the flux in the SQUIDs place additional demands on cooling power, introduce crosstalk and may complicate the integration with three-dimensional (3D) architectures[11,12]. In superconductor–semiconductor JJs, E_J can be controlled by local capacitively coupled gates[4,5,13], which opens up the possibility to tune and modulate f_Q without the need for current-biased flux lines. Although this eliminates sensitivity to flux noise, charge fluctuations can couple to the qubit frequency via the gate electrode and dielectric substrate near the JJ. Recent experiments on nanowire (NW) gatemons, however, demonstrated relaxation and coherence times that exceed 20 μs and 4 μs, respectively[14,15], which mitigates this concern in the near term. More immediate challenges to building NW-based architectures, however, are viable ways to scale and the upper limit on E_J imposed by their ~100 nm dimensions.

In this work, we realize scalable superconductor–semiconductor JJs that use the 2DEG heterostructure shown schematically in Fig. 1b. The 2DEG is formed in an InAs quantum well (green) encapsulated between InGaAs barriers (light grey). We leverage recent breakthroughs in using in situ epitaxy of Al (blue) on III–V semiconductors[16] to obtain a pristine high-transparency superconductor–semiconductor interface between a 50 nm thick layer of superconducting aluminium and the 2DEG. Superconducting correlations are induced in the 2DEG by electron–hole (e–h) conversion at this interface, a process known as Andreev reflection. A JJ is formed by selectively etching away a narrow strip of the Al top layer to leave proximitized banks on either side of a normal region (see Methods for more fabrication details). Cooper pairs traverse this normal region via e–h pairs that repeatedly reflect from each side and form bound states between the proximitized 2DEG. E_J is modulated by the voltage applied to the top gate, which changes the carrier density in the normal region of the junction. Semi-insulating (Fe-doped) InP is used as a host substrate for the 2DEG buffer layer, which is etched away before patterning the qubit island and microwave control circuitry. Figure 1c shows a false-coloured scanning electron micrograph of the JJ.

First, we demonstrate that, unlike NW gatemons, 2DEG gatemons can be fabricated deterministically with a superior reproducibility. We fabricated three devices (S1, S2 and S3) each of which hosted six qubits with the junction width w increasing from 0.3 to 2.6 μm (labelled Q1–Q6). To extract the E_J of the as-fabricated
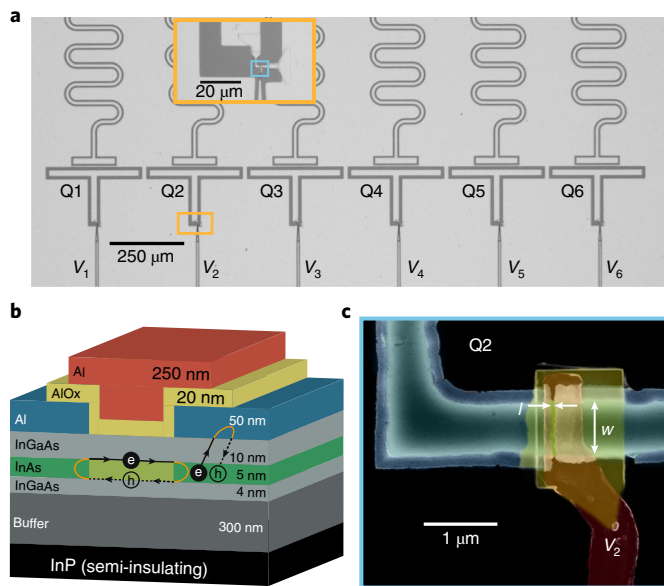
Fig. 1 | 2DEG gatemon. a, Optical micrograph of a six qubit device. The 2DEG JJ is shunted by the T-shaped island to the surrounding ground plane and coupled to individual readout cavities. The gate voltage V_j changes the qubit frequency of Qj. **b,** Schematic of the wafer stack. The InAs quantum well (green) is proximitized by Andreev reflection (orange) at the highly transparent interface with the Al (blue). Cooper pairs traverse the JJ (light green) by Andreev bound states confined between the proximitized 2DEG regions under the Al (dark green). **c,** False-coloured scanning electron micrograph of the gate-controlled 2DEG JJ of width w and length l. At the edge of the mesa the Al overhangs due to an undercut when etching the semiconductor buffer.

qubits, the corresponding cavity frequency (f_c) is measured before any voltage is applied to the gate. Due to vacuum fluctuations in the electric field between the cavity and qubit, the cavity is Lamb shifted from its bare resonance frequency by $\chi = g_{cav}^2/\Delta_Q$, where $\Delta_Q/2\pi = f_c - f_Q$ is the qubit–cavity detuning. The cavity coupling strength, $g_{cav}/2\pi \approx 100$ MHz, is extracted from qubit spectroscopy in the dispersive limit (details are given below) and, together with numerical simulations for C ($E_C/h \approx 230$ MHz), allows us to estimate E_J. Figure 2a plots the extracted E_J as a function of w for all the measured qubits. The data show that E_J increases for wider junctions, as expected with an increasing number of modes that participate in Cooper pair transport[17]. We omit the data from the widest JJs of 2.6 μm (Q6), as the Lamb shift is too small to extract E_J. Such a precise control of E_J on a design parameter w represents an important step towards engineering scalable superconductor–semiconductor quantum information processors, improving on previous realizations where w was limited by the 1D character of NWs[18].

Next, we show all-electric control by tuning the qubit transition frequency in Fig. 2b. We operate in the transmon regime, $E_J/E_C \approx 70$–130, and read out the qubit dispersively ($g_{cav} \ll |\Delta_Q|$) (ref. [19]). Using two-tone spectroscopy, we drive a single qubit (Q3) and identify its frequency as a function of gate voltage from the state-dependent push on the cavity. The frequency $f_{Q3}(V_3)$ is monotonic over a wider voltage range than for NWs[4,15] and can be tuned by $\Delta f \approx 1$ GHz for 1 V applied to the gate (V_j corresponds to the voltage applied to jth qubit Qj). The dependence of qubit frequency on gate voltage can be optimized by changing the thickness of the dielectric layer and using 2DEGs with different field-effect mobilities. Higher-mobility 2DEGs might also allow further improvements to the reproducibility of the junction characteristics, and so simplify the control of larger-scale devices.

We next demonstrate the basic operations of individual qubits using time-domain manipulation and readout. Phase-controlled microwave pulses with drive frequency f_d are applied either via the cavity readout feedline or separately through the JJ top gate. The rotation about the x axis of the Bloch sphere is performed by applying the pulse for a time τ_{Rabi} and reading out the state via the cavity (pulse sequence, Fig. 2c). Plotting the probability to be in $|1\rangle$, $P_{|1\rangle}$, as a function of τ_{Rabi} and f_d, reveals Rabi oscillations (Fig. 2c), characteristic of the qubit rotation. These data are used to calibrate the pulse times and amplitudes to rotate by π and $\pi/2$ around the x axis (X and $X/2$ pulses, respectively). We next show the coherent accumulation of the dynamical phase by a controlled rotation of the qubit around the z axis. Figure 2d shows the pulse sequence that comprises a resonant ($f_d = f_Q$) $X/2$ pulse, a gate pulse with amplitude ΔV_3 and duration τ_{Ramsey} and a second $X/2$ pulse. When $\Delta V_3 = 0$ the qubit and drive are phase locked, so the two $X/2$ pulses rotate the qubit to the $|1\rangle$ state. With increasing ΔV_3, the qubit rotates around the z axis relative to the drive. Although further experiments, such as randomized benchmarking, are required to establish fidelities, these data establish the high degree of control afforded by electrostatically coupled gates.

To measure the relaxation time, T_1, an X pulse excites the qubit (Fig. 3a, blue pulse sequence) and $P_{|1\rangle}$ is plotted as a function of τ, the time delay before readout. The probability decreases exponentially due to relaxation. Fitting the decay (blue) yields $T_1 = 1.1$ μs. Assuming the qubit lifetime limits the precision of single qubit gates, for a microwave pulse time of 20 ns we estimate an upper bound of 99.4% for the fidelity[20]. To extract the dephasing time T_2^*, two slightly detuned $X/2$ pulses are applied (Fig. 3a, black pulse sequence), separated by the delay time τ. A fit to the decay of the resulting Ramsey fringes (Fig. 3a inset) gives a dephasing time of $T_2^* = 400$ ns. To reduce the inhomogeneous dephasing due to low-frequency noise, we perform a Hahn echo sequence that comprises a refocusing X pulse between two $X/2$ pulses (Fig. 3a, red). The extracted $T_{2,echo} = 2.2$ μs $\approx 2T_1$ indicates that 2DEG gatemon dephasing is dominated by low-frequency noise[21]. Figure 3b shows T_1 as a function of qubit frequency. Relaxation times vary between 0.2 and 2 μs and fluctuate strongly with f_Q (the spectrum is plotted in the inset Fig. 3b). Owing to their periodicity, we attribute these fluctuations to on-chip modes, which is consistent with previous results from devices that lack crossover wire bonds.

An estimate for the dielectric loss of the qubit capacitor can be made using a test resonator coupled to the same feedline ($f_{res} = 5.35$ GHz), which shows an internal quality factor $Q \approx 6.4 \times 10^4$ at a low photon number. Using the expression $T_1 = Q/(2\pi f_Q)$, we expect the relaxation time due to dielectric loss to follow the black dashed line in Fig. 3b[22]. The agreement between the measured T_1 times and this upper bound suggests the qubit lifetime is, indeed, limited by dielectric loss. Similar Q values are obtained on pure semi-insulating InP substrates, which suggests that the presence of the 2DEG does not introduce additional loss. Test resonators on GaAs and GaSb substrates showed significantly lower Q values, consistent with previous reports[23,24]. Suitable solutions to reduce microwave loss compatible with InP-based 2DEGs include deep-etching trenches[25] and flip-chip techniques used to host the qubit island on a low-loss substrate such as Si (ref. [12]). From the measured slope df/dV of 1 GHz V^{-1} and $T_2^* = 400$ ns, we estimate an equivalent root-mean-squared (r.m.s.) gate voltage noise of ~0.5 mV (ref. [26]). Previous r.m.s. gate-voltage fluctuation measurements of ~8 μV in III–V semiconductors[26] suggest that $T_2^* \sim 25$ μs could be achieved. This implies that the prospects are good for obtaining coherence times comparable with state-of-the-art flux-tunable transmons for which $T_1 \approx 30$ μs and $T_2^* \approx 5$ μs (refs [9,10,27]).

Finally, we coherently swap excitations using the capacitive coupling between neighbouring qubits. The monotonicity over a range of 0.5 GHz of the qubit spectra established in Fig. 2 is useful for tuning
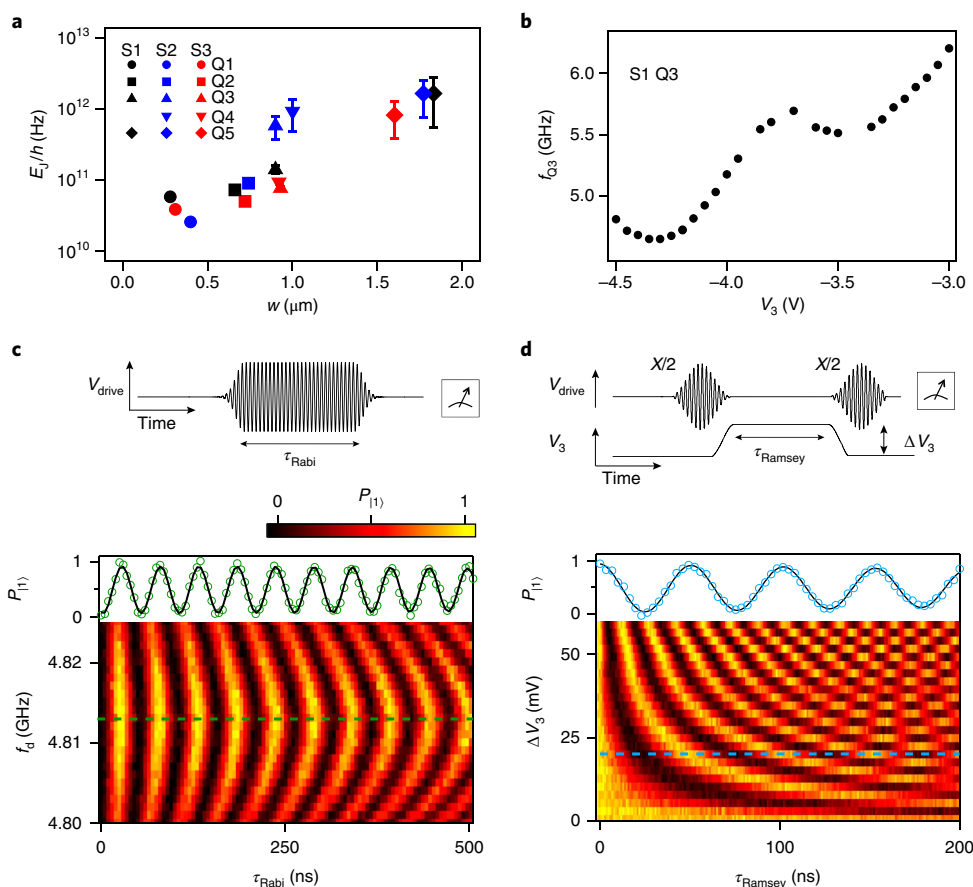
Fig. 2 | Coherent qubit manipulation. a, Overview of E_J as a function of w for three devices, S1, S2 and S3, at zero gate voltage. **b**, Frequency of S1 Q3 as a function of gate voltage. **c**, Coherent Rabi oscillations performed at $V_3 = -4.5\,V$ by applying the microwave pulse sequence shown in the upper panel. The main panel shows qubit oscillations as a function of the qubit drive frequency f_d and τ_{Rabi}, and the inset shows a cut at the resonance frequency. The solid line is a fit to the data using a Gaussian-damped sinusoid. **d**, Coherent qubit rotations around the z axis. The qubit is positioned on the equator with an $X/2$ pulse followed by a gate pulse with amplitude ΔV_3 and duration τ_{Ramsey} and finally rotated back by an $X/2$ pulse (upper panel). The main panel shows the coherent Z oscillation as a function ΔV_3 and τ_{Ramsey}, and the inset shows a cut at $\Delta V_3 = 20\,mV$.
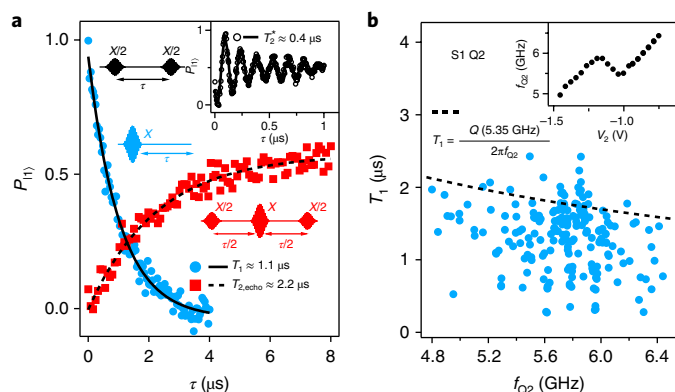

Fig. 3 | Coherence times. a, Lifetime measurement for S1 Q2 (blue) with qubit resonance frequency $f_{Q2} \approx 5\,GHz$. We performed a Hahn echo experiment to determine $T_{2,echo}$ (red). The black lines (solid and dashed) are exponential fits. The pulse sequences for dephasing ($T_{2,echo}$) (red) and relaxation (T_1) measurements are shown next to their respective data. The inset shows a Ramsey experiment which was performed to determine T_2 for Q2 with the pulse sequence shown next to the inset (black). The solid line in the inset is a fit to the data using an exponentially damped sinusoid. **b**, Relaxation time measurements as a function of qubit frequency. The dashed line indicates the limit on the qubit lifetime for a quality factor $Q \approx 6.4 \times 10^4$. The inset shows the spectrum for Q2.

adjacent qubits into resonance with each other. The signature of qubit–qubit coupling is a mutual push on the bare qubit frequencies due to hybridization. To detect this push, the qubits Q2 and Q3 are driven and read out through the feedline and their respective cavities. For clarity, the signals detected from both cavities are added to yield the sum V_Σ. Figure 4a shows V_Σ as a function of the qubit drive and V_2. As expected, due to the absence of crosstalk, there are two peaks in V_Σ as a function of f_d, only one of which (Q2) is tuned by V_2. When tuned onto resonance, the qubits anticross and a splitting of $2g/2\pi \approx 12\,MHz$ between the two hybridized states is observed, where g is the qubit–qubit coupling strength. Figure 4b shows the pulse sequence that exploits the anticrossing to transfer coherently an excitation between Q2 and Q3, the starting point for preparing arbitrary two-qubit states. With the two qubits detuned by ~140 MHz and Q3 idling, Q2 is prepared in $|1\rangle$. A gate pulse is then applied for time τ_{swap} and brings Q2 into resonance with Q3[28]. Note that here the microwave pulses are applied through the gate line, which demonstrates qubit manipulation using a single control line per qubit. We emphasize that such single-gate control of rotations around the x, y and z axes is an important advantage of voltage-controlled qubits. The probability that an excitation swaps between the qubits depends on τ_{swap} and the pulse amplitude ΔV_2. Figure 4c shows the typical chevron pattern of swap oscillations[29]. The lower panel in Fig. 4c shows $P_{|1\rangle}$ for each qubit separately. The anticorrelation confirms that the excitation transfers between Q2 and Q3 and demonstrates the possibility of generating entangled states using 2DEG gatemon
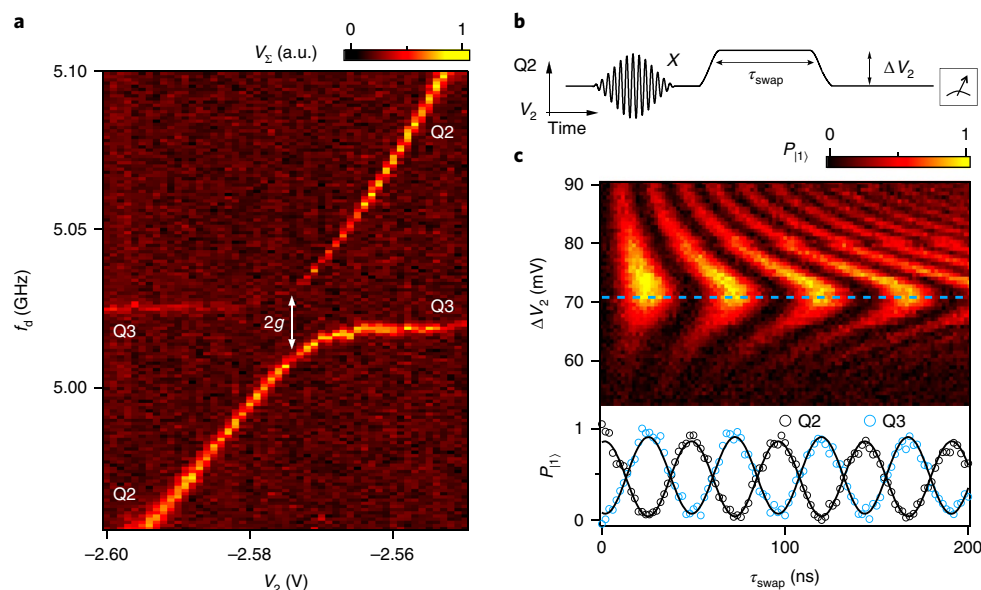
Fig. 4 | Coherent two-qubit interaction. a, Measurement of the avoided level crossing between Q2 and Q3. The sum of the normalized heterodyne readout amplitude V_Σ for both qubits is shown as a function of qubit drive and V_2. **b**, Pulse sequence to probe the coherent coupling between the qubits. With Q2 and Q3 detuned, Q3 is prepared in the ground state and an X pulse prepares Q2 in $|1\rangle$. A gate pulse of amplitude ΔV_2 brings Q2 close to or in resonance with Q3 for time τ_{swap}. **c**, The $|1\rangle$ state probability, $P_{|1\rangle}$, for Q3 as a function of ΔV_2 and τ_{swap}. Lower panel: $P_{|1\rangle}$ for both Q2 and Q3 at $\Delta V_2 \approx 71$ mV, which brings the two qubits into resonance.

qubits. From sinusoidal fits (Fig. 4b, solid lines) an interaction rate of $2g/2\pi = 14$ MHz is extracted, in good agreement with electrostatic simulations that yield $2g/2\pi \approx 15$ MHz for $f_Q = 5$ GHz.

In summary, we have demonstrated that planar semiconductor materials and superconducting microwave circuits are compatible technologies that can be readily integrated while they maintain quantum coherence. This opens new possibilities for highly integrated quantum processors with on-chip components. Through a combination of geometry and applied voltages, E_J can be tailored to simultaneously suit qubits and peripheral control circuits that require a higher E_J, such as tunable couplers[2,30] and on-chip microwave sources[31], and develop naturally into the 3D architectures required to implement fault-tolerant processing[12,32]. Moreover, as 2DEG gatemons represent a perfect quantum counterpart to semiconductor-based cryogenic classical control logic[33–35], they take the first step towards realizing a scalable all-electric hybrid superconductor–semiconductor quantum processor.

Methods

Methods, including statements of data availability and any associated accession codes and references, are available at https://doi.org/10.1038/s41565-018-0207-y.

References

1. Koch, J. et al. Charge-insensitive qubit design derived from the Cooper pair box. *Phys. Rev. A.* **76**, 042319 (2007).
2. Chen, Y. et al. Qubit architecture with high coherence and fast tunable coupling. *Phys. Rev. Lett.* **113**, 220502 (2014).
3. Castellanos-Beltran, M. A. & Lehnert, K. W. Widely tunable parametric amplifier based on a superconducting quantum interference device array resonator. *Appl. Phys. Lett.* **91**, 083509 (2007).
4. Larsen, T. W. et al. A semiconductor nanowire-based superconducting qubit. *Phys. Rev. Lett.* **115**, 127001 (2015).
5. de Lange, G. et al. Realization of microwave quantum circuits using hybrid superconducting–semiconducting nanowire Josephson elements. *Phys. Rev. Lett.* **115**, 127002 (2015).
6. Vincenzo, D. The physical implementation of quantum computation. Preprint at https://arxiv.org/abs/quant-ph/0002077 (2000).
7. Clarke, J. & Wilhelm, F. K. Superconducting quantum bits. *Nature* **453**, 1031–1042 (2008).
8. Sheldon, S., Magesan, E., Chow, J. M. & Gambetta, J. M. Procedure for systematically tuning up cross-talk in the cross-resonance gate. *Phys. Rev. A.* **93**, 060302 (2016).
9. Hutchings, M. D. et al. Tunable superconducting qubits with flux-independent coherence. *Phys. Rev. Appl* **8**, 044003 (2017).
10. Kelly, J. et al. State preservation by repetitive error detection in a superconducting quantum circuit. *Nature* **519**, 66–69 (2015).
11. Neill, C. et al. A blueprint for demonstrating quantum supremacy with superconducting qubits. *Science* **360**, 195–199 (2018).
12. Rosenberg, D. et al. 3D integrated superconducting qubits. *Quantum Inf.* **3**, 42 (2017).
13. Kjaergaard, M. et al. Transparent semiconductor–superconductor interface and induced gap in an epitaxial heterostructure Josephson junction. *Phys. Rev. Appl.* **7**, 034029 (2017).
14. Luthi, F. et al. Evolution of nanowire transmons and their quantum coherence in magnetic field. *Phys. Rev. Lett.* **120**, 100502 (2018).
15. Casparis, L. et al. Gatemon benchmarking and two-qubit operations. *Phys. Rev. Lett.* **116**, 150505 (2016).
16. Shabani, J. et al. Two-dimensional epitaxial superconductor–semiconductor heterostructures: a platform for topological superconducting networks. *Phys. Rev. B* **93**, 155402 (2016).
17. Kringhøj, A. et al. Anharmonicity of a superconducting qubit with a few-mode Josephson junction. *Phys. Rev. B* **97**, 060508 (2018).
18. Abay, S. High critical-current superconductor-InAs nanowire–superconductor junctions. *Nano. Lett.* **12**, 5622 (2012).
19. Wallraff, A. et al. Strong coupling of a single photon to a superconducting qubit using circuit quantum electrodynamics. *Nature* **431**, 162–167 (2004).
20. O'Malley, P. J. J. et al. Qubit metrology of ultralow phase noise using randomized benchmarking. *Phys. Rev. Appl.* **3**, 044009 (2015).
21. Bylander, J. et al. Noise spectroscopy through dynamical decoupling with a superconducting flux qubit. *Nat. Phys.* **7**, 565–570 (2011).
22. Barends, R. et al. Coherent Josephson qubit suitable for scalable quantum integrated circuits. *Phys. Rev. Lett.* **111**, 080502 (2013).
23. Krupka, J., Hartnett, J. G. & Piersa, M. Permittivity and microwave absorption of semi-insulating InP at microwave frequencies. *Appl. Phys. Lett.* **98**, 112112 (2011).
24. Frey, T. S. *Interaction between Quantum Dots and Superconducting Microwave Resonators.* PhD thesis, ETH Zurich (2013).
25. Bruno, A. et al. Reducing intrinsic loss in superconducting resonators by surface treatment and deep etching of silicon substrates. *Appl. Phys. Lett.* **106**, 182601 (2015).

26. Dial, O. E. et al. Charge noise spectroscopy using coherent exchange oscillations in a singlet–triplet qubit. *Phys. Rev. Lett.* **110**, 146804 (2013).
27. Rol, M. A. et al. Restless tuneup of high-fidelity qubit gates. *Phys. Rev. Appl.* **7**, 041001 (2017).
28. Majer, J. et al. Coupling superconducting qubits via a cavity bus. *Nature* **449**, 443–447 (2007).
29. Hofheinz, M. et al. Synthesizing arbitrary quantum states in a superconducting resonator. *Nature* **459**, 546–549 (2009).
30. Casparis, L. et al. Voltage-controlled superconducting quantum bus. Preprint at https://arxiv.org/abs/1802.01327 (2018).
31. Cassidy, M. C. et al. Demonstration of an a.c. Josephson junction laser. *Science* **355**, 939–942 (2017).
32. Versluis, R. et al. Scalable quantum circuit and control for a superconducting surface code. *Phys. Rev. Appl.* **8**, 034021 (2017).
33. Ward, D. R., Savage, D. E., Lagally, M. G., Coppersmith, S. N. & Eriksson, M. A. Integration of on-chip field-effect transistor switches with dopantless Si/SiGe quantum dots for high-throughput testing. *Appl. Phys. Lett.* **102**, 213107 (2013).
34. Al-Taie, H. et al. Cryogenic on-chip multiplexer for the study of quantum transport in 256 split-gate devices. *Appl. Phys. Lett.* **102**, 243102 (2013).
35. Hornibrook, J. M. et al. Cryogenic control architecture for large-scale quantum computing. *Phys. Rev. Appl.* **3**, 024010 (2015).

Acknowledgements

Author contributions

T.W., C.T., S.G., G.C.G. and M.J.M. grew the proximitized 2DEG. M.K., L.C., C.M.M. and K.D.P designed the experiment. L.C., M.R.C., A.K., N.J.P., T.W.L., and K.D.P. prepared the experimental set-up. L.C. and M.R.C. fabricated the devices and performed the experiment. L.C., M.R.C., M.K., A.K., T.W.L., F.K., C.M.M. and K.D.P. analysed the data and prepared the manuscript.

Competing interests

The authors declare no competing interests.

Additional information

Reprints and permissions information is available at www.nature.com/reprints.

Correspondence and requests for materials should be addressed to K.D.P.

Publisher's note: Springer Nature remains neutral with regard to jurisdictional claims in published maps and institutional affiliations.

Methods

The sample. Separate transport characterization shows that the 2DEGs exhibit a Hall mobility of approximately 2,000 cm^2 V^{-1} s^{-1} and an induced gap of 200 µeV. The qubits were fabricated by first wet etching a mesa for the qubit JJ. The width w of the JJ was defined by the mesa etch. The JJ was then formed by selectively wet etching an $l \sim 100$ nm long segment of the ~50 nm thick Al. A 20 nm thick AlOx layer (yellow in Fig. 1b,c) was deposited as a gate dielectric, followed by the evaporation of an Al top gate (red in Fig. 1b). The heterostructure and buffer were removed almost everywhere on the chip, to leave a mesa region a few micrometres large to form the active region of the qubit. The qubit islands, gate lines and readout cavities were defined in a lift-off process with a 100 nm Al layer. Finally, the epitaxial Al layer on top of the mesa and the microwave circuit were connected in a contact step. For each qubit, E_C/h is determined by the capacitance of the T-shaped Al island to the surrounding ground plane and designed to be ~230 MHz.

All qubits were coupled to individual $\lambda/4$ superconducting cavities with resonant frequencies separated by 50 MHz and centred around 7.25 GHz. All six cavities were coupled to a common feed line[22].

Qubit manipulation and readout. All measurements presented in the paper were performed in a cryogen-free dilution refrigerator with a base temperature below 50 mK. The sample was mounted inside an Al box to suppress magnetic fluctuations. This box was placed inside a Cu box used to mount the sample at the mixing chamber plate of the refrigerator. Both boxes were closed but not light tight and further surrounded by a cylindrical cryoperm shield, which was also thermally anchored to the mixing chamber.

The qubit was initialized in the $|0\rangle$ state by waiting for much longer than the relaxation time T_1. To manipulate a single qubit, one coaxial line and a DC line were used: the coaxial line was filtered by a Minicircuits VLF-320 low-pass filter and an ECCOSORB filter to reduce the noise while allowing for gate pulses. At high frequencies (>2 GHz), the filter attenuated by roughly 20 dB, which allowed direct driving of the qubit. The d.c. line was filtered with a resistor–capacitor filter and added with a bias tee at low temperature. For the X microwave control as well as readout, the pulses were shaped through IQ modulation of the microwave source and using an arbitrary waveform generator channel for I (in-phase component of the waveform) and Q (quadrature component). For readout, the signal line was heavily attenuated (60 dB) to reduce both the thermal occupation of the resonator and noise to the sample. After passing through a magnetically shielded isolator, a travelling wave parametric amplifier[36], another magnetically shielded isolator, a cryogenic Low Noise Factory high-electron-mobility transistor amplifier and another amplification stage at room temperature, the qubit readout signals were mixed down to intermediate frequencies with a local oscillator, before sampling and performing digital homodyne detection to extract the cavity magnitude response. Qubit state measurements were obtained by averaging over ~1,000 experimental runs. We used the raw Rabi oscillation data for the qubit ensemble state assignments[4]. The data in Fig. 2a were acquired with a vector network analyser. The data in all the other figures were acquired using heterodyne detection in the dispersive regime. For Fig. 4 we combined two drives with frequencies close to the resonance frequencies of the cavities of Q2 and Q3 on the signal line.

Data availability. The data that support the plots within this paper and other findings of this study are available from the corresponding author upon reasonable request.

References

36. Macklin, C. et al. A near-quantum-limited Josephson traveling-wave parametric amplifier. *Science* **350**, 307–310 (2015).